Decoupling translational and rotational effects on the phase synchronization of rotating helices

Jonathan H. Tu, Murat Arcak, and Michel M. Maharbiz

Decoupling translational and rotational effects on the phase synchronization of rotating helices

Jonathan H. Tu,[*] Murat Arcak, and Michel M. Maharbiz

University of California Berkeley

(Dated: [To be inserted by editor])

The locomotion of swimming microorganisms often relies on synchronized motions; examples include the bundling of flagella and metachronal coordination of cilia. It is now generally accepted that such behavior can result from hydrodynamic interactions alone. In this paper we consider the interactions between two side-by-side rigid helices driven by constant torques. We use the method of regularized Stokeslets to simulate an end-pinned model, in which restoring forces and torques are applied at one end of each helix. This allows us to decouple the respective effects of translation and rotation on phase synchronization. We find that while translational freedom leads to synchrony, rotational freedom can result in either synchrony or antisynchrony, depending on the stiffness of the system. In addition, we characterize the nature of the physical mechanisms driving these behaviors, focusing on the individual effects of each applied force and torque. For translational freedom, there is a single underlying mechanism in which the interaction forces indirectly influence the helix rotation rates. Multiple mechanisms are at play for rotational freedom: the interaction torques may exert either direct or indirect influence depending on stiffness. These characterizations are important to the future development of reduced-order models, which should capture not only the expected end behaviors (synchrony or antisynchrony), but also the nature of the driving mechanisms.

PACS numbers: 47.63.Gd,47.63.mf,87.16.Qp

I. INTRODUCTION

Due to their small size, microscopic swimming organisms live in highly viscous environments where inertial effects are neglibible. The familiar strategies used by larger swimming organisms and aquatic vehicles are generally ineffective at these small length scales. Instead, microswimmers propel themselves using nonreciprocal motions. Familiar examples include the corkscrew-like rotation of helical prokaryotic flagella, the whip-like undulation of eukaryotic flagella, and the rowing-like power/recovery strokes of cilia. In microorganisms with multiple appendages, these motions are often coordinated. For instance, the bundling and unbundling of flagella in *Escherichia coli* leads to their well-known run-and-tumble behavior [1, 2]. We refer the reader to [3] for a general review of flagellar and ciliary swimming strategies.

In this work, we investigate the physical mechanisms that drive phase synchronization between rigid flagella. Such interactions may be responsible for the unusual motility strategy utilized by *Mixotricha paradoxa*, which cannot produce thrust by itself [4]. Instead, its movement is driven by a surface coating of symbiotic spirochetes. Not only do these spirochetes rotate about their axes, but they also undulate in a transverse direction. The result is a transverse traveling wave reminiscent of those commonly observed in cilia. A better understanding of inter-flagella interactions may explain why this particular organism has evolved such a unique swimming strategy.

It may also suggest novel thrust production strategies for the design of artificial microswimmer robots.

While it is possible that microswimmers actively coordinate their appendages, it is now well-established that such coordination may result solely from passive hydrodynamic effects. For example, G. I. Taylor's pioneering study showed that small-amplitude traveling waves in infinite sheets tend to synchronize [5]. Detailed numerical simulations of cilia found a similar tendency toward coordination [6, 7]. In both cases, synchronous behavior was shown to be energetically favorable [5, 7, 8]. Studies using simplified oscillator models have identified a number of potential driving mechanisms, including flexibility [9], time dependence [10], and compressibility[11].

Many studies of inter-flagellar interactions focus on bundling behavior [12–16]. We instead focus on phase synchronization, building on the work presented in [17] and [18]. The former used slender body theory to show that rigid helices constrained to purely axial rotation will not synchronize. The latter used numerical simulations to explore the effects of a minimally flexible model in which the ends of each helix were placed in harmonic traps. It was observed that some degree of flexibility is necessary for synchronization to occur.

The present work expands on [17] and [18] using the method of regularized Stokeslets to simulate the interactions of rigid helices. Our end-pinned model allows us to decouple the effects of translation from those of rotation. We find that the effects of pure rotation are much more complex than those of pure translation; their combination results in even more complicated behavior. Translational freedom results in synchronous behavior and is driven by a single mechanism. Rotational freedom can produce either synchronous or antisynchronous behavior;

---
[*] jhtu@berkeley.edu

many physical mechanisms are at play. In each case we focus on identifying the particular role of each applied force and torque, characterizing the roles as direct or indirect. These characterizations will inform the development of reduced-order models, which should not only reproduce expected end behaviors (synchrony or antisynchrony), but should also do so using realistic mechanisms.

We emphasize that our analysis is based on solutions of the Stokes equations, a set of partial differential equations, and not a model system of ordinary differential equations (ODEs). Such ODE models are featured prominently in the coupled oscillator literature but often rely on simplistic coupling mechanisms that cannot capture the behaviors described in this work [19–21]. More advanced ODE models have been proposed for the study of interactions between cilia [9, 22–24]. The coupling terms in these models are derived from hydrodynamic principles and are thus more realistic, but to simplify the governing equations each cilium is modeled as a single sphere. In contrast, our simulations fully resolve all geometries and do not simplify the fluidic interactions between solid bodies.

The remainder of this work is structured as follows: Sec. II introduces the method of regularized Stokeslets. We describe our end-pinned model and its governing equations in Sec. III. Results are presented in Sec. IV. Finally, we summarize our findings and suggest directions for future work in Sec. V.

II. NUMERICAL METHODS

The characteristic length and velocity scales for swimming microorganisms are extremely small, especially with respect to the viscosity of their fluid environments. Letting ρ be the fluid density, $\bar{U}$ a characteristic velocity, $\bar{R}$ a characteristic length, and ν the kinematic fluid viscosity, the Reynolds numbers $\text{Re} \triangleq \bar{U}\bar{R}/\nu$ for microswimmers are nearly zero; for an *E. coli* $\text{Re} \approx 10^{-5}$. As such, their fluid mechanics are governed by the Stokes equations, shown below in non-dimensional form:

$$\begin{aligned} \mathbf{0} &= -\nabla p + \nabla^2 \mathbf{u} + \mathbf{f} \\ \mathbf{0} &= \nabla \cdot \mathbf{u}, \end{aligned} \quad (1)$$

where p is the pressure, $\mathbf{u}$ is the velocity, and $\mathbf{f}$ is an external force exerted on the fluid. Note that these equations are linear and independent of time. Consequently, low Reynolds number flows are reversible and reciprical motions cannot generate thrust, as famously pointed out by Purcell [25].

The velocity field induced by an external point force $\mathbf{f}^*$ applied at $\boldsymbol{\xi}^*$ is given by a fundamental solution of the Stokes equations known as a *Stokeslet* [26–28]:

$$\mathbf{u}_s(\boldsymbol{\xi}; \boldsymbol{\xi}^*, \mathbf{f}^*) = \frac{\mathbf{f}^*}{8\pi r} + \frac{[\mathbf{f}^* \cdot (\boldsymbol{\xi} - \boldsymbol{\xi}^*)](\boldsymbol{\xi} - \boldsymbol{\xi}^*)}{8\pi r^3}, \quad (2)$$

where $\boldsymbol{\xi}$ is the spatial coordinate in $\mathbb{R}^3$ and $r = \|\boldsymbol{\xi} - \boldsymbol{\xi}^*\|$. Equation (1) is linear so we can use superposition to compute the velocity field generated by a distribution of point forces. However, the singularity in Eq. (2) at $\boldsymbol{\xi} = \boldsymbol{\xi}^*$ makes it impossible to evaluate the induced velocity field at the forcing locations, which is often required to enforce boundary conditions.

The *method of regularized Stokeslets* [29, 30] avoids this problem by smoothing point forces into force distributions using a cutoff function $\phi_\varepsilon(\boldsymbol{\xi})$ that satisfies

$$\int_{\mathbb{R}^3} \phi_\varepsilon(\boldsymbol{\xi}) \, \mathrm{d}\boldsymbol{\xi} = 1$$
$$\lim_{\varepsilon \to 0} \phi_\varepsilon = \delta,$$

where δ is the Dirac delta function and ε is a parameter describing the extent of the distribution. For the cutoff function

$$\phi_\epsilon(r) = \frac{15\varepsilon^4}{8\pi(r^2 + \varepsilon^2)^{7/2}},$$

the *regularized Stokeslet* is an exact solution of the Stokes equations that induces a velocity field

$$\begin{aligned} \mathbf{u}_{s,\varepsilon}(\boldsymbol{\xi}; \boldsymbol{\xi}^*, \mathbf{f}^*) =& \frac{\mathbf{f}^*(r^2 + 2\varepsilon^2)}{8\pi(r^2 + \varepsilon^2)^{3/2}} \\ &+ \frac{[\mathbf{f}^* \cdot (\boldsymbol{\xi} - \boldsymbol{\xi}^*)](\boldsymbol{\xi} - \boldsymbol{\xi}^*)}{8\pi(r^2 + \varepsilon^2)^3}. \end{aligned} \quad (3)$$

As $\varepsilon \to 0$ we recover Eq. (2). For an error analysis regarding the choice of ε, see [30].

To describe the motion of a body in Stokes flow, we discretize the body surface and place a regularized Stokeslet at each discretization point. The velocity at a set of n_u points $\boldsymbol{\xi}_k$ can be computed by summing the effect of each regularized Stokeslet:

$$\mathbf{u}(\boldsymbol{\xi}_k) = \sum_{j=1}^{n_s} \mathbf{u}_{s,\varepsilon}(\boldsymbol{\xi}_k; \boldsymbol{\xi}_j^*, \mathbf{f}_j^*), \quad k = 1, \dots, n_u \quad (4)$$

where $\boldsymbol{\xi}_j^*$ is the location of the jth discretization point, $\mathbf{f}_j^*$ is the force applied at that point, and n_s is the number of discretization points. In three dimensions the result is a $3n_u \times 3n_s$ matrix equation relating forces to velocities:

$$\begin{bmatrix} \mathbf{u}(\boldsymbol{\xi}_1) \\ \vdots \\ \mathbf{u}(\boldsymbol{\xi}_{n_u}) \end{bmatrix} = \begin{bmatrix} & \mathbf{G}(\boldsymbol{\xi}, \boldsymbol{\xi}^*, \varepsilon) & \end{bmatrix} \begin{bmatrix} \mathbf{f}_1^* \\ \vdots \\ \mathbf{f}_{n_s}^* \end{bmatrix} \quad (5)$$

If the forcing is known, we can evaluate the right-hand side of Eq. (5) directly to compute the velocity at any point in the flow field. We can also use the no-slip boundary condition to solve for unknown forces by choosing $n_u = n_s$ and evaluating the velocities at the surface boundary points. In other words, we choose the collocation points to coincide with the locations of the regularized Stokeslets. $\mathbf{G}(\boldsymbol{\xi}, \boldsymbol{\xi}^*, \varepsilon)$ is then $3n_s \times 3n_s$ and can be inverted to compute unknown boundary forces from known boundary velocities.

III. HELIX MODEL

In this work we investigate the effects of translational and rotational motion on the phase dynamics of a pair of helices. The two helices have identical geometries and are driven by torques of equal and constant magnitude. All restoring forces and torques acting on a helix are applied at one of its ends. This can be thought of as a crude model in which a rigid flagellum is attached to its flagellar motor by a flexible proximal hook. The following sections describe this geometry and the corresponding governing equations in detail.

A. Geometry

The centerline coordinates for a helix aligned along the z axis are given by

$$
\begin{aligned}
x_c &= R\cos(2\pi z_c/\lambda) \\
y_c &= R\sin(2\pi z_c/\lambda), \\
&0 \le z_c \le L
\end{aligned} \tag{6}
$$

where R is the coil radius, λ is the pitch, and L is the length. For a finite-thickness helix the filament radius a is an additional parameter. We describe the orientation of the helix using three vectors $\boldsymbol{\rho}$, $\boldsymbol{\alpha}$, and $\boldsymbol{\beta}$ (each an element of $\mathbb{R}^3$), as illustrated in Fig. 1. $\boldsymbol{\rho}$ points from a reference point O to one end of the helix axis, which we label O' and think of as a local origin for the helix. $\boldsymbol{\alpha}$ is a unit vector that points in the direction of the helix axis. $\boldsymbol{\beta}$ is a unit vector that points from the local origin to the near tip of the helix. $\boldsymbol{\alpha}$ and $\boldsymbol{\beta}$ are orthogonal by definition, so the nine elements of $\boldsymbol{\rho}$, $\boldsymbol{\alpha}$, and $\boldsymbol{\beta}$ describe six degrees of freedom. The phase of the helix is defined by the tip vector $\boldsymbol{\beta}$. In this work we consider helices whose axes are nominally aligned with the negative x axis. As such we define the helix phase θ as the angle between the y axis and the projection of $\boldsymbol{\beta}$ onto the yz plane, as shown in Fig. 2.

All lengths are nondimensionalized by the coil radius, so $R = 1$. The other parameter values are chosen to match those for bacterial flagella: $a = R/16$, $\lambda = 11R$, and $L = 2.8\lambda$ [31, 32]. Figure 3 shows an illustration of two such helices placed a distance $\delta = 10R$ apart. To reduce computational costs, we do not explicitly discretize
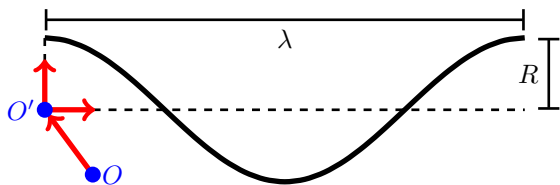

FIG. 1. (Color online) Schematic showing helix position and orientation (not to scale).
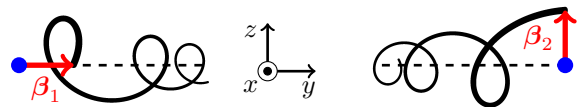

FIG. 2. (Color online) Schematic showing how helix phase is defined. The helices are shown in a perspective view with each helix axis parallel to the x axis (out of the page). Helix 1 has a phase $\theta_1 = 0$ and helix 2 has a phase $\theta_2 = \pi/2$.
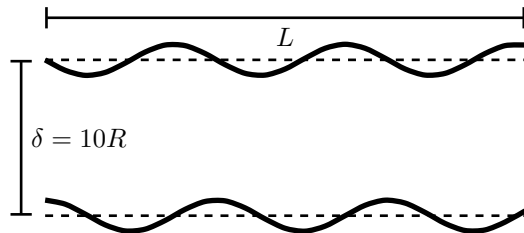

FIG. 3. Schematic of helix geometry used in simulations (to scale). The local origins are shown at their equilibrium positions and and the helix phase difference is $\Delta\theta = \pi/2$.

the surfaces of the helices. Instead, we place $n_s = 130$ regularized Stokeslets along the helix centerlines and tune the regularization parameter ε to account for the finite filament radius [33]. We find that $\varepsilon = 0.5L/n_s$ reproduces the behavior for $a = R/16$ with high accuracy.

B. Dynamics

Each helix is driven by a torque

$$
\mathbf{T}_{\mathrm{dr},i} = T_{\mathrm{dr}}^* \boldsymbol{\alpha}_i, \tag{7}
$$

where $i = 1, 2$ is the helix index. The driving torque has a constant magnitude T_{dr}^* and is aligned with the instantaneous helix axis. This matches the observation that flagellar motors operate at constant torque [34, 35].

We apply restoring forces and torques to keep each helix close to its equilibrium position and orientation. Let $\boldsymbol{\rho}$ and $\boldsymbol{\rho}_i^*$ be the instantaneous and equilibrium positions of the ith helix, respectively. The restoring force on the ith helix is proportional to its displacement from the equilibrium:

$$
\mathbf{F}_{\mathrm{spr},i} = -k_{\mathrm{tr}}(\boldsymbol{\rho}_i - \boldsymbol{\rho}_i^*). \tag{8}
$$

Similarly, let $\boldsymbol{\alpha}_i^*$ be the direction of the ith helix axis at equilibrium. The restoring torque

$$
\mathbf{T}_{\mathrm{spr},i} = -k_{\mathrm{rot}}\sin^{-1}(\|\boldsymbol{\alpha}_i^* \times \boldsymbol{\alpha}_i\|)\frac{\boldsymbol{\alpha}_i^* \times \boldsymbol{\alpha}_i}{\|\boldsymbol{\alpha}_i^* \times \boldsymbol{\alpha}_i\|} \tag{9}
$$

is proportional to the angle between the equilibrium and instantaneous helix axes.

The dynamics of each helix are given by

$$\frac{\mathrm{d}}{\mathrm{d}t}\boldsymbol{\rho}_i = \mathbf{U}_i$$
$$\frac{\mathrm{d}}{\mathrm{d}t}\boldsymbol{\alpha}_i = \boldsymbol{\Omega}_i \times \boldsymbol{\alpha}_i, \qquad (10)$$
$$\frac{\mathrm{d}}{\mathrm{d}t}\boldsymbol{\beta}_i = \boldsymbol{\Omega}_i \times \boldsymbol{\beta}_i$$

where $\mathbf{U}_i$ and $\boldsymbol{\Omega}_i$ are the linear and angular velocity vectors for helix i, respectively. Due to the linearity of the Stokes equations [Eq. (1)], the velocity vectors must satisfy

$$\begin{bmatrix} \mathbf{F}_1 \\ \mathbf{T}_1 \\ \mathbf{F}_2 \\ \mathbf{T}_2 \end{bmatrix} = \begin{bmatrix} & & \\ & \mathbf{R} & \\ & & \end{bmatrix} \begin{bmatrix} \mathbf{U}_1 \\ \boldsymbol{\Omega}_1 \\ \mathbf{U}_2 \\ \boldsymbol{\Omega}_2 \end{bmatrix}, \qquad (11)$$

where $\mathbf{F}_i$ and $\mathbf{T}_i$ are the net force and torque on the ith helix, respectively, and $\mathbf{R}$ is known as the resistance matrix [36].

The value of $\mathbf{R}$ varies nonlinearly with the positions and orientations of the helices and must be computed at each instant in time. We do so column by column. The first column of $\mathbf{R}$ is computed by solving Eq. (5) for the net forces and torques exerted by the fluid on the helices when $\mathbf{U}_1 = (1,0,0)$ and $\mathbf{U}_2 = \boldsymbol{\Omega}_1 = \boldsymbol{\Omega}_2 = (0,0,0)$; the other columns are computed similarly. If there are constraints on the helix motions, then we can eliminate certain columns of $\mathbf{R}$. For example, if the x position of helix 1 is fixed, then the first row and column of $\mathbf{R}$ play no role and do not need to be computed. The truncated velocity vectors are then related to truncated force and torque vectors by the truncated $\mathbf{R}$ matrix.

Together, Eqs. (10) and (11) comprise a differential algebraic equation (DAE). We solve the DAE numerically as follows, recalling that the helix positions and orientations are known at all times:

1. Compute the driving torques from the helix axis vectors via Eq. (7). In this work we set the torque magnitude to $T_{\mathrm{dr}}^* = 92.78$. This is the value that causes an isolated helix constrained to pure axial rotation to rotate at a unit rate. (Preliminary results show that varying the the torque magnitude has negligible effect on the qualitative nature of the helix interactions.)

2. Compute the restoring forces from the helix position vectors via Eq. (8).

3. Compute the restoring torques from the helix axis vectors via Eq. (9).

4. Sum the driving and restoring torques to get the net torque.

5. Compute the resistance matrix $\mathbf{R}$ column by column, as described above. Neglect rows and columns as necessary according to motion constraints.

6. Solve Eq. (11) for the linear and rotational velocity vectors by inverting $\mathbf{R}$.

7. Use the velocity vectors to numerically integrate Eq. (10) and advance forward by a timestep.

8. The geometric constraints on $\boldsymbol{\rho}_i$, $\boldsymbol{\alpha}_i$, and $\boldsymbol{\beta}_i$ may no longer hold due to numerical integration errors. Enforce these constraints at each timestep by orthogonalizing $\boldsymbol{\beta}_i$ with respect to $\boldsymbol{\alpha}_i$, then scaling $\boldsymbol{\rho}_i$, $\boldsymbol{\alpha}_i$, and $\boldsymbol{\beta}_i$ to each have unit length (for $i = 1, 2$).

The simulation results presented in Sec. IV are integrated using a forward Euler scheme with $\Delta t = 0.05$, which corresponds to approximately 125 timesteps per helix rotation. We find that our the results are converged with respect to the timestep and compare well to results obtained with a fourth-order Runge-Kutta scheme.

IV. RESULTS AND DISCUSSION

In this section, we present the results of numerical simulations for helix interactions under various motion constraints. For each case we identify the effects of applied forces and torques on the observed behaviors. This provides a data-based characterization of the physical mechanisms at play. We find that in some cases inter-helix interactions play a direct role, while in others they play an indirect role. We also investigate how the stiffness of the system affects the observed behavior.

The three cases we consider are free axial rotation [Fig. 4(b)] with: 1) sprung transverse translation [Fig. 4(c)], 2) sprung transverse rotation [Fig. 4(d)], and 3) combined sprung transverse translation and sprung transverse rotation. It is well established that under free axial rotation with no other motion, rigid helices maintain their initial phase difference and do not synchronize [17, 18]. Our simulations confirm this, thus we do
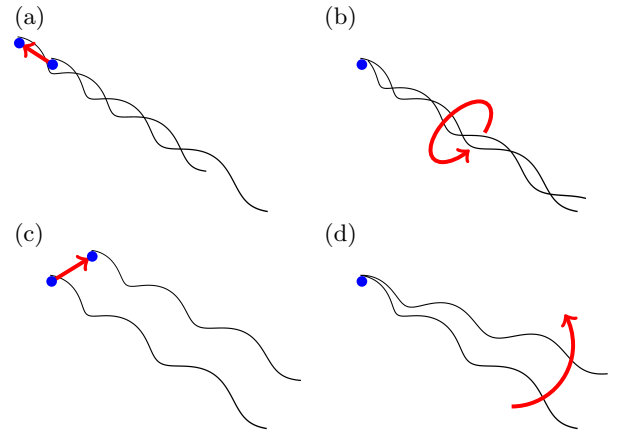

FIG. 4. (Color online) Illustration of constrained helix motions. (a) Axial translation; (b) axial rotation; (c) transverse translation; (d) transverse rotation.

not consider this case further. Our simulations also show that sprung axial translation [Fig. 4(a)] has little effect on the phase dynamics, whether alone or in combination with other motions. Thus we do not consider this degree of freedom either.

We group translations in the two transverse directions together in one case because this is most consistent with a biologically-inspired model. In our end-pinned model, restoring forces and torques are applied at one end of each helix, as if a rigid flagellum were connected to its flagellar motor by a flexible proximal hook. As the flagellum rotates, the proximal hook will turn with it. Then if the proximal hook can provide flexibility in one transverse direction, as it rotates it will also provide flexibility in the other. For similar reasons, we also group both directions of transverse rotation together.

A. Transverse translation

First, we consider the effect of sprung transverse translation. A constant driving torque is applied to each helix along its axis, which is forced to remain parallel to the x axis at all times. This generates transverse forces that cause each helix to undergo pure translation in addition to axial rotation. That is, the helices translate with their axes remaining parallel to the x axis [as in Fig. 4(c)]. These transverse translations are resisted by linear spring forces, which keep the helices near their respective equilibrium positions.

Figure 5 shows the evolution of the phase difference for a translational spring constant $k_{\rm tr} = 100$. Over long time scales, we see a slow sigmoidal change in the phase difference, which starts at 0.994π (179°) and decreases toward zero. There are also small-amplitude oscillations that occur on a fast time scale matching that of the individual helix rotations. (These can be seen more clearly in Fig. 6.) We find that these general characteristics are independent of the initial helix phases, which affect only the phase of the fast dynamics. Similarly, changes in the spring constant affect only the synchronization rate.
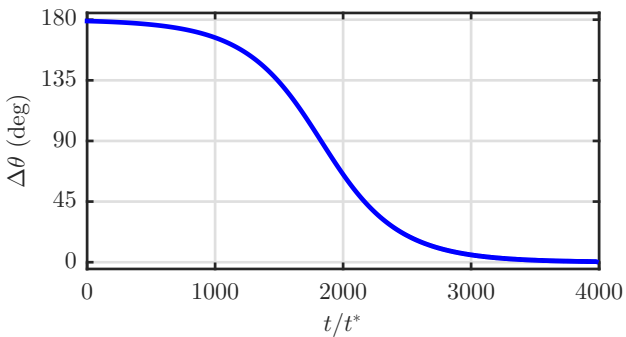
In order for the phases to synchronize, the helix rotation rates must differ, with the lagging helix rotating faster than the leading helix. Recall that free axial rotation alone does not yield phase synchronization [17, 18]. Then the difference in rotation rates must be driven by the influence of transverse interaction forces. As we show below, this effect is an indirect one: the interaction forces modulate the amplitude of the self forces, which in turn modulate the rotation rates.

Since only rotation about the x axis is allowed, the rotation rate of helix i is given by $\Omega_{x,i}$. We can invert Eq. (11) to write

$$\begin{bmatrix}\mathbf{U}_1\\\mathbf{\Omega}_1\\\mathbf{U}_2\\\mathbf{\Omega}_2\end{bmatrix} = \begin{bmatrix} & \mathbf{M} & \end{bmatrix}\begin{bmatrix}\mathbf{F}_1\\\mathbf{T}_1\\\mathbf{F}_2\\\mathbf{T}_2\end{bmatrix}, \qquad (12)$$

where $\mathbf{M} = \mathbf{R}^{-1}$ is known as the mobility matrix. Then the rotation rate is a linear combination

$$\Omega_{x,i} = \sum_{j=1}^{2}\mathbf{M}_{\Omega_{x,i}/\mathbf{F}_{yz,j}}\mathbf{F}_{yz,j} + \mathbf{M}_{\Omega_{x,i}/\mathbf{T}_{x,j}}\mathbf{T}_{x,j}.$$

We refer to the terms where $i = j$ as those due to *self forces* and *self torques*; those where $i \neq j$ are due to *interaction forces* and *interaction torques*. We use this decomposition to analyze the way in which interaction forces induce phase synchronization.

Taking the difference $\Delta\Omega_x = \Omega_{x,2} - \Omega_{x,1}$, we group terms to identify the individual contributions to the difference in helix rotation rates. For instance, the contribution of self torques is given by

$$\Delta\Omega_x^{\mathbf{T}_x,{\rm self}} = \mathbf{M}_{\Omega_{x,2}/\mathbf{T}_{x,2}}\mathbf{T}_{x,2} - \mathbf{M}_{\Omega_{x,2}/\mathbf{T}_{x,1}}\mathbf{T}_{x,1}.$$

We then integrate to find the contribution of self torques to the difference in helix phases:

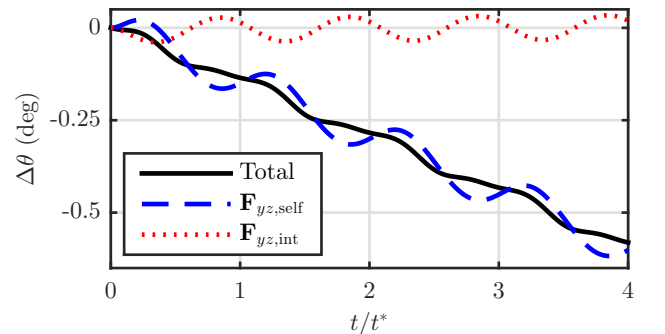$$\Delta\theta_x^{\mathbf{T}_x,{\rm self}} = \int \Delta\Omega_x^{\mathbf{T}_x,{\rm self}}\,{\rm d}t.$$

FIG. 6. (Color online) Comparison of self and interaction force contributions to the change in phase difference for $k_{\rm tr} = 100$. While self forces drive a long-term decrease in phase difference, the interaction force contribution oscillates around zero. (The contributions of self and interaction torques, not shown, also oscillate around zero, with even smaller amplitude than that of the interaction force.)

FIG. 5. (Color online) Time history of helix phase difference for $k_{\rm tr} = 100$, showing convergence to a synchronized state. Time is normalized by the rotation period of an isolated helix.

Similar expressions can be written for the contributions of self forces, interaction forces, and interaction torques.

Figure 6 shows a comparison of the self and interaction force contributions to the phase difference. (Here we consider a trajectory starting from an initial phase difference of $\pi/2$, where the synchronization rate is fastest.) We see that the self forces have a direct effect on phase synchronization: their contribution clearly decreases at the same rate as the overall phase difference. In contrast, the interaction force contribution oscillates about zero, affecting the phase and amplitude of the fast dynamics but not the trajectory of the slow synchronizing dynamics. Thus we conclude that the interaction forces do not directly influence phase synchronization. (The contributions of the self and interaction torques also oscillate about zero, with smaller amplitudes than the interaction force contribution; they have no direct influence either.)

What then, is the role of interaction forces? By process of elimination they must affect the translational dynamics. This is corroborated by a comparison of the individual elements of the mobility matrix [see Eq. (12)]. The elements relating interaction forces to translational velocities are on the order of 10^{-3}. In comparison, the elements relating interaction forces to rotational velocities are on the order of 10^{-4}. We see evidence of this effect in the y displacement of each helix from its equilibrium position, shown in Fig. 7. If the helices did not interact, these curves would differ by only a phase shift. Instead, we see that the curves also differ in amplitude, which is critical to the synchronization mechanism.

Figure 8 shows the contribution of the y component of the self force to each helix's rotation rate. (Similar behavior is observed for the z component.) The shaded regions show times during which the contribution to helix 1 (the leading helix) is greater than that to helix 2 (the lagging helix). During these times helix 1 is slowing down relative to helix 2 and the system is moving toward synchrony. (Recall that the helix axes are aligned with the negative x axis, meaning that $\Omega_{x,i}$ is a negative quantity.) In the unshaded regions the opposite is true. It is clear from Fig. 8 that an amplitude difference is neces-
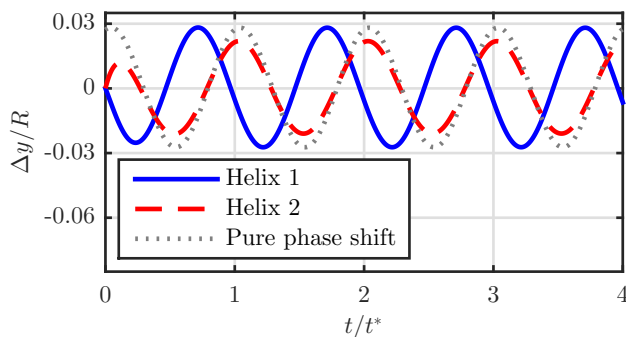
sary. Without one, the synchronizing regions would not dominate and the phase difference would simply oscillate, rather than tending toward synchrony.

One question remains: why is it the lagging helix that experiences smaller displacements? The answer lies in the symmetry breaking caused by the phase difference. When the force on the leading helix (helix 1) is greatest, the helices are relatively close together and their interactions are stronger. The opposite is true when the lagging helix (helix 2) experiences its maximum force. As a result, the leading helix suppresses the motion of the lagging helix more than the other way around.

The physical mechanism driving phase synchronization can thus be summarized as follows: the presence of interaction forces alters the translational motion of each helix, with the lagging helix undergoing smaller amplitude displacements. As a result, the spring forces exerted on each helix differ. These differing forces contribute to the synchronizing phase difference not as interaction forces, but as self forces. We then say that for free axial rotation with sprung transverse translation, interaction forces have an indirect effect on phase synchronization.

As we vary the spring constant, the interaction forces continue to play the same indirect role, but the rate of synchronization changes. We measure this using the 5% settling time $t_{s,5}$, which we define to be the time it takes for the phase difference to decrease from $\pi/2$ to only 5% of that value. (We find no qualitative changes in our results if we use other thresholds, such as 1% or 10% settling times.) Figure 9 shows that the settling time varies non-monotonically with spring constant. At first, increases in stiffness reduce the settling time, but past a certain threshold stiffness and settling time increase together. The latter behavior is to be expected: in the limit of infinite stiffness there is no translational motion and no synchronization should occur [17, 18].

To understand this variation in the synchronization rate, we consider the decomposition of the translational
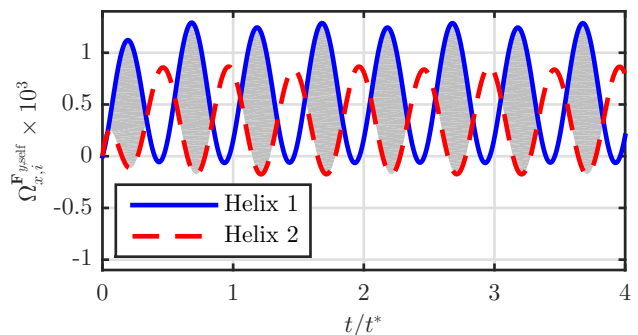

FIG. 7. (Color online) Comparison of y displacement for $k_{\text{tr}} = 100$. Helix 1 (the leading helix) experiences larger amplitude displacements than helix 2 (the lagging helix).

FIG. 8. (Color online) Self force contributions (y component only) to rotation rate for $k_{\text{tr}} = 100$. Shaded regions indicate times during which helix 1 (leading) slows down relative to helix 2 (lagging). ($\boldsymbol{\Omega}_i$ is parallel to the negative axis so positive contributions slow down the helices.) The amplitude difference between the two curves results in net synchronization.
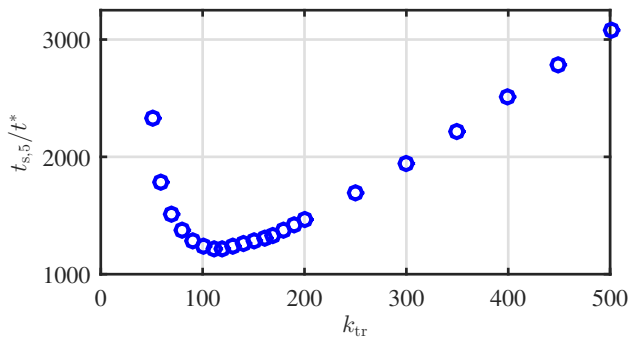
FIG. 9. (Color online) 5% settling time from an initial phase difference of $\pi/2$, as a function of translational spring constant. Note that the variation is non-monotonic.

velocity into contributions from forces and torques. Figure 10 shows the contributions to the y velocity of helix 1, for three different spring constants. Comparing the blue dashed curves across the three subfigures, we see that the torque contribution does not vary with spring constant. The corresponding curves for helix 2 (not shown) differ from those for helix 1 by only a phase shift. Since we know that phase synchronization is driven by differences in the *amplitude* of each helix's translational motion, we conclude that the variation in synchronization rate must result from variations in the force contributions. (The torque contributions alone would yield phase-shifted velocities and thus phase-shifted displacements.)

For small spring constants, we see from Fig. 10(a) that the force contribution has a small amplitude relative to the torque contribution. Then the amplitude of the overall velocity cannot differ much from that of the torque contribution. As such, the difference in amplitudes between the helices cannot be large; both must remain close to the same value. The result is a slow synchronization rate.

In contrast, for large spring constants the force contribution is large. However, it is out of phase with the torque contribution, resulting in small total velocities [see Fig. 10(c)]. Since the velocity amplitude for each helix is small, so is their difference. Again, the result is slow synchronization, though the underlying mechanism is different than that for small spring constants.

Figure 10(b) shows a comparison of the contributions for a fast synchronization case. We see that at this intermediate spring constant, the force contributions and total velocities are both relatively large. As a result, the difference in velocity amplitudes between helices can also be large, allowing for faster synchronization.

B. Transverse rotation

We now consider the effect of sprung transverse rotation, focusing on differences from the effects of sprung transverse translation. As before, a constant torque is
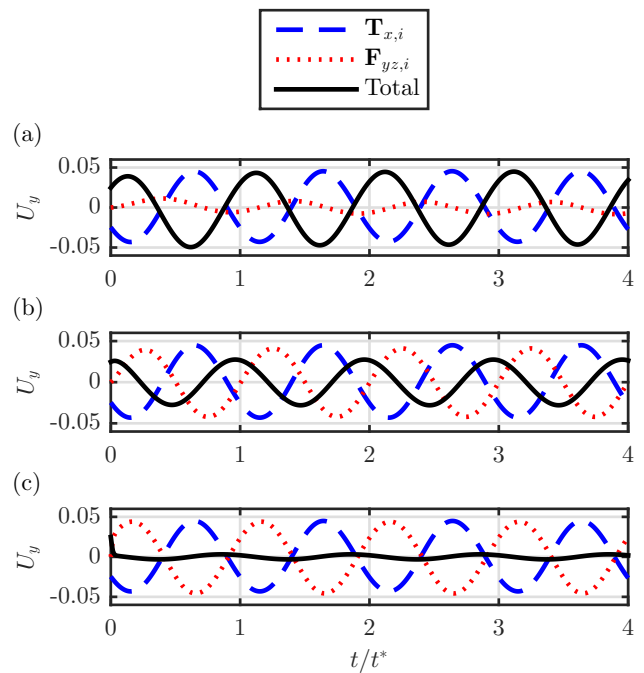

FIG. 10. (Color online) Component contributions to y velocity for helix 1. (a) $k_{tr} = 10$; (b) $k_{tr} = 100$; (c) $k_{tr} = 1000$. For small spring constants, the force contribution only modifies the torque contribution by a small amount. For large spring constants the modification is large but out of phase, resulting in small total velocities. For intermediate spring constants, we get both large modifications and large total velocities.

applied along each helix axis, but now the axes are allowed to tilt and precess and may not remain aligned with the x axis. Restoring torques are applied to force each axis back toward its equilibrium direction (parallel to the x axis); each spring torque is proportional to the angle between the x axis and the instantaneous helix axis.

Compared to sprung translation, sprung rotation yields a much richer set of behaviors. Figure 11 shows two typical trajectories (for $k_{rot} = 20,000$ and $k_{rot} = 50,000$). Similar to the sprung translation case, there are slow sigmoidal changes in the phase difference along with fast small-amplitude oscillations. However, for sprung rotation we observe both synchronized and antisynchronized final states.

Here we define the 5% settling time as the time required for the phase difference change by $0.95\pi/2$ in either direction. Figure 12 shows how this value varies with spring constant. We see that for low spring constants the dynamics tend toward antisynchrony; for high spring constants we observe synchrony instead. In both the synchronous and antisynchronous regimes the variation is non-monotonic. As before, in the limit of infinite stiffness we observe the expected increase in settling time.

Why does sprung rotation produce such a wide range of behavior? Unlike with sprung translation, there are multiple physical mechanisms at play and the dominant mechanism varies with the spring constant. To identify
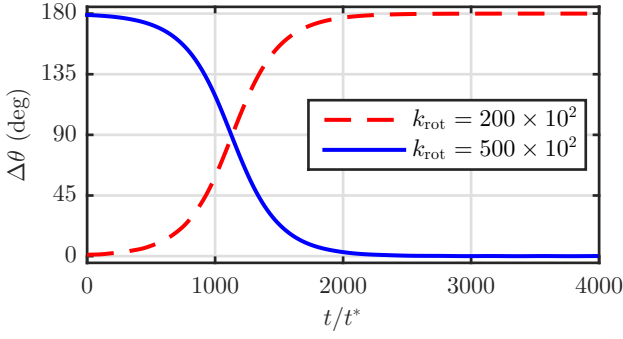
FIG. 11. (Color online) Time history of helix phase difference. Time is normalized by the rotation period of an isolated helix. We see that for transverse rotation, both antisynchronous and synchronous behaviors are possible.
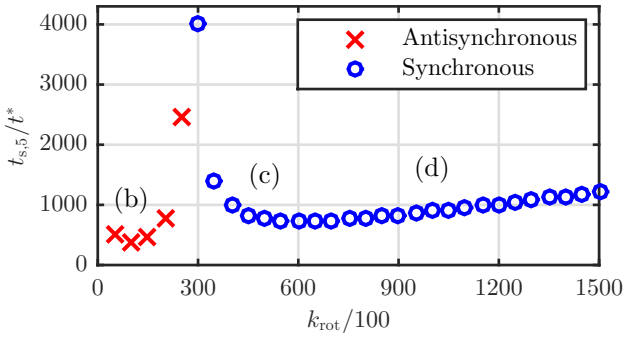

FIG. 12. (Color online) 5% settling time from an initial phase difference of $\pi/2$, as a function of translational spring constant. We observe both antisynchronous and synchronous behavior. Labels correspond to cases further illustrated in Fig. 13.

FIG. 13. (Color online) Comparison of dominant contributions to $\Omega_{x,1}$ for different spring constants. (a) $k_{\rm rot} = 100$; (b) $k_{\rm rot} = 10,000$; (c) $k_{\rm rot} = 50,000$; (d) $k_{\rm rot} = 100,000$. Note that the component responsible for the phase behavior changes. For instance, axial self torque is only important for $k_{\rm rot} = 100$. Furthermore, the nature of the contribution can change. For $k_{\rm rot} = 10,000$ transverse self torques drive the system toward antisynchrony while for $k_{\rm rot} = 50,000$ the opposite is true.

these mechanisms, we again decompose the rotation rate about the x axis into contributions from self and interaction torques about the x, y, and z axes, respectively. We note that for rotational motion, we cannot simply integrate Ω_x to get the phase θ; to get the exact phase we must account for all components of the angular velocity. However, for these helix geometries the helix axes do not depart far from the x axis and Ω_x dominates the angular velocity. Then we can expect the phase dynamics to be dominated by the contribution from Ω_x, and it is still instructive to consider its integral.

Figure 13 shows a comparison of the dominant contributions to Ω_x (integrated over time) for four spring constants: $k_{\rm rot} = 100$ (slow antisynchrony), $k_{\rm rot} = 10,000$ (fast antisynchrony), $k_{\rm rot} = 50,000$ (slow synchrony), and $k_{\rm rot} = 100,000$ (slow synchrony). We see that the dominant contributions change from case to case. At $k_{\rm rot} = 100$ [Fig. 13(a)], torques about the x axis push the system toward antisynchrony. This is opposed by the effect of transverse self torques. As the spring constant increases, the helix axes begin to align more closely with the x axis and the effect of x torques becomes negligible. (The only source of x torque is the driving torque, which
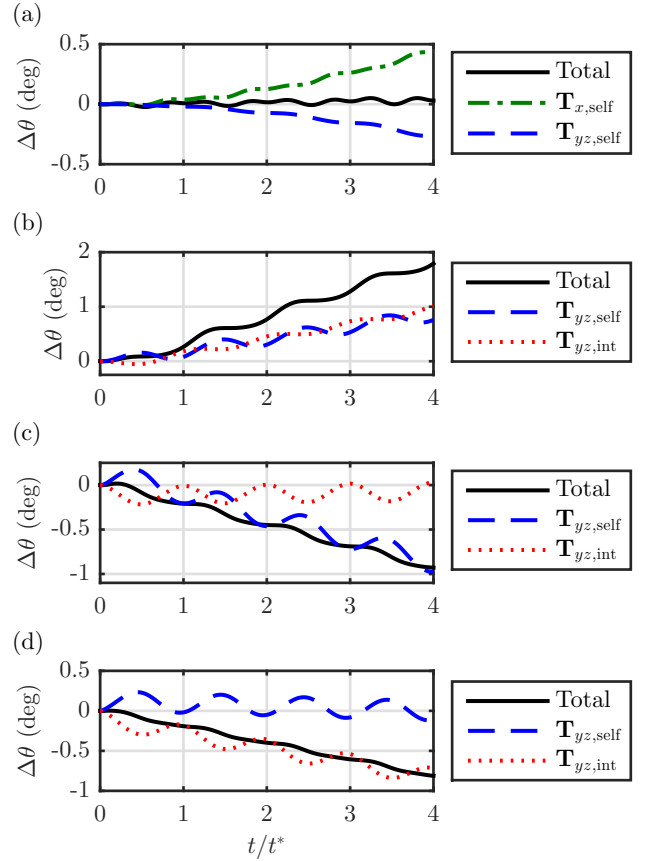
is now nearly constant.) At $k_{\rm rot} = 10,000$ all transverse torques, both self and interaction, drive the system to antisynchrony [Fig. 13(b)]. Further increases in spring constant result in synchronous behavior. At first, this is the result of transverse self torques alone [Fig. 13(c)]. However, for even higher spring constants the transverse self torques play a much smaller role and transverse interaction torques dominate instead [Fig. 13(d)]. We note that of these four cases, the contribution of interaction torques is direct for $k_{\rm rot} = 10,000$ and $k_{\rm rot} = 100,000$ and indirect for the others.

C. Combined

When both transverse rotation and transverse translation are allowed, the resulting behavior is more complex than a simple superposition. Figure 14 shows the 5% settling time observed as a function of the two spring con-
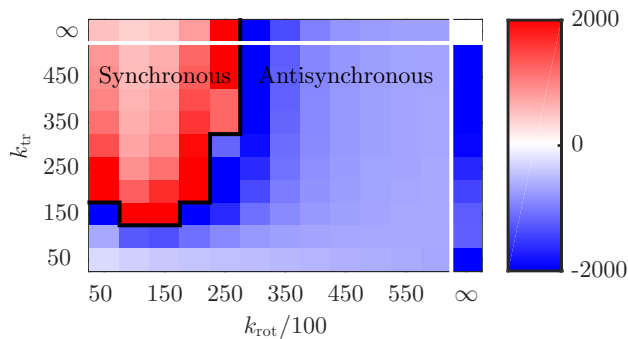
FIG. 14. (Color online) Normalized settling time for combined rotation and translation. Synchronous settling times are shown as negative. Antisynchronous settling times are shown as positive.

FIG. 15. (Color online) Settling time as a function of $k_{\rm rot}$, for various fixed values of $k_{\rm tr}$. For a stiff spring with $k_{\rm tr} = 500$ the behavior resembles that for an infinitely stiff spring. In contrast, for a flexible spring with $k_{\rm tr} = 100$ the behavior at small values of $k_{\rm rot}$ is fundamentally different.

stants $k_{\rm tr}$ and $k_{\rm rot}$. We see that both synchronous and antisynchronous behaviors are observed. When both spring constants are small the translational effects dominate and we observe synchrony, rather that the antisynchrony that results from rotational effects alone. In contrast, when the translational spring is stiff but the rotational spring is not, we are able to achieve antisynchrony, which is never observed with translational effects alone. There is also an interesting "re-entrant" behavior at $k_{\rm tr} = 150$, where the system tends from synchrony to antisynchrony and then back to synchrony as $k_{\rm rot}$ increases.

Figure 15 shows a comparison of settling times as a function of $k_{\rm rot}$ alone, for various fixed values of $k_{\rm tr}$. For a relatively stiff translational spring with $k_{\rm tr} = 500$, the behavior is similar to that observed for an infinitely stiff translational spring. The main difference is that the antisynchronization rates are slower while the synchronization rates are faster. This is consistent with the observation that translation alone results in synchrony, as if the effects of pure translation were being added to those of pure rotation. However, for a more flexible translational spring with $k_{\rm tr} = 100$, this reasoning doesn't hold. Instead we see a fundamentally different behavior where there is actually synchronization in place of antisynchronization at low $k_{\rm rot}$. Furthermore, these synchronization rates are faster than those observed in Fig. 9 for an infinitely stiff translational spring. Thus the addition of translational flexibility not only changes the behavior from antisynchronous to synchronous, but it also accelerates the synchronizing effects.

As before, to elucidate this behavior we consider the contributions of the self and interaction forces and torques to the phase difference. Figure 16 shows the dominant contributions for combined translation and rotation with $k_{\rm tr} = 100$ and $k_{\rm rot} = 10,000$, translation alone with $k_{\rm tr} = 100$, and rotation alone with $k_{\rm rot} = 10,000$. It is clear that the dominant contributions are fundamentally different when translation is combined with rotation. For instance, the self force provides less than $1°$ phase decrease for translation alone but over $2°$ de-

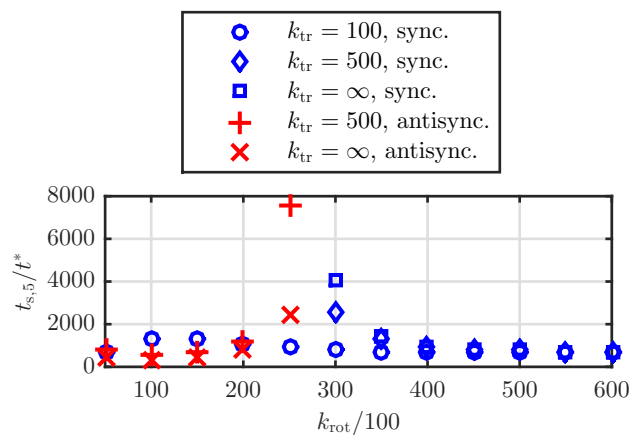crease for translation with rotation. Similarly, the growth rates and oscillation amplitudes of the transverse torque contributions are different in Fig. 16(a) compared to Fig. 16(c). Rather than a simple superposition, the presence of transverse rotation has an indirect effect in altering the self force contribution; similarly the transverse forces have an indirect effect in altering the contributions of the transverse torques.

V. CONCLUSIONS AND FUTURE WORK

We have characterized the respective effects of translation and rotation on helix phase synchronization using numerical solutions of the Stokes equations computed with the method of regularized Stokeslets. We showed that for free axial rotation with sprung transverse translation, the interaction forces play an indirect role. Out-of-phase helices experience asymmetric interactions that cause the leading helix to undergo larger translational displacements compared to the lagging helix. As a result, larger spring forces are exerted on leading helix than on the lagging helix. The differing force amplitudes affect the phase dynamics not as interaction forces, but as self forces, and drive the system toward synchrony.

In contrast, we found that free axial rotation with sprung transverse rotation can produce either synchrony or antisynchrony, depending on the spring constant. This is due to the richness in the underlying physical mechanisms: the particular force or torque dominating the phase dynamics changes with the spring constant. For instance, axial self torques contribute to the phase dynamics only at low spring constants. At higher spring constants only transverse torques play a significant role. However, even for higher spring constants there is variation. In some cases it is transverse self torques that dom-
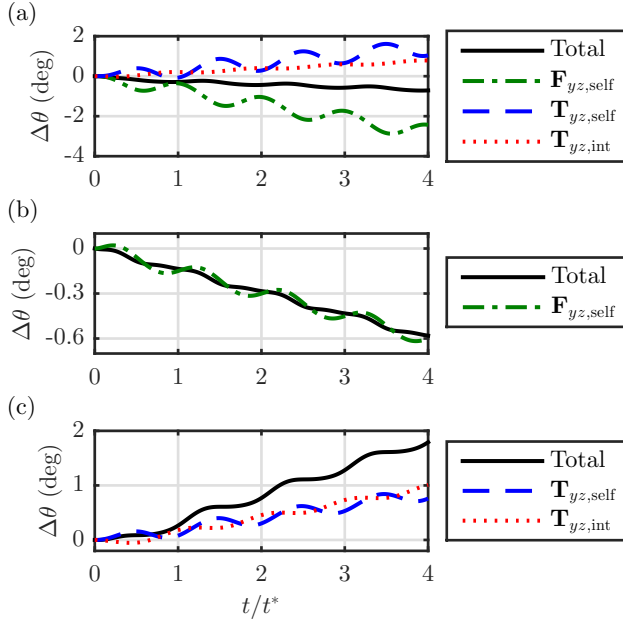
FIG. 16. (Color online) Comparison of dominant contributions to phase difference, for different motion constraints. (a) Both transverse translation and transverse rotation ($k_{\mathrm{tr}} = 100$, $k_{\mathrm{rot}} = 10,000$); (b) transverse translation only ($k_{\mathrm{tr}} = 100$); (c) transverse rotation only ($k_{\mathrm{rot}} = 10,000$). The behavior for rotation combined with translation is not a simple superposition. When both translation and rotation are allowed, the contributions have different dynamics (e.g., growth rates, oscillation amplitudes).

inate while in others it is transverse interaction torques.

For some spring constants the interaction torques drive the system toward antisynchrony while for others the opposite is true.

When transverse translation and rotation are combined, the behavior is even more complex. In the limit of infinite spring constants we recover the behavior of pure translation or pure rotation; differences can be explained with simple superposition arguments. These arguments fail to explain the complex behavior for small spring constants, where the translational and rotational effects interact with each other. For instance, in the presence of rotation the self force contribution to phase synchrony is enhanced compared to the contribution for translation alone.

The fundamental characterizations presented here will inform our future efforts to develop reduced-order models that not only produce the correct end behaviors (synchrony or antisynchrony), but also do so using mechanisms faithful to the true dynamics. Such models will enable the study of much larger numbers of helices (perhaps thousands or more). As our models become more detailed, we will start to incorporate the effect of parameter variations. This could include changes in the inter-helix spacing or the helix geometries. In parallel work, we plan to investigate how interactions between flexible helices compare to those between rigid ones.

ACKNOWLEDGMENTS

[1] H. C. Berg and D. A. Brown, Nature **239**, 500 (1972).
[2] H. C. Berg, E. coli *in motion* (Springer-Verlag, New York, 2004).
[3] C. Brennen and H. Winet, Annu. Rev. Fluid Mech. **9**, 339 (1977).
[4] L. R. Cleveland and A. V. Grimstone, P. R. Soc. B-Biol. Sci. **159**, 668 (1964).
[5] G. Taylor, P. R. Soc. A-Math. Phy. **209**, 447 (1951).
[6] S. Gueron, K. Levit-Gurevich, N. Liron, and J. J. Blum, P. Natl. Acad. Sci. USA **94**, 6001 (1997).
[7] J. Elgeti and G. Gompper, P. Natl. Acad. Sci. USA **110**, 4470 (2013).
[8] S. Gueron and K. Levit-Gurevich, P. Natl. Acad. Sci. USA **96**, 12240 (1999).
[9] T. Niedermayer, B. Eckhardt, and P. Lenz, Chaos **18** (2008), 10.1063/1.2956984.
[10] M. Theers and R. G. Winkler, Phys. Rev. E **88** (2013), 10.1103/PhysRevE.88.023012.
[11] M. Theers and R. G. Winkler, Soft Matter **10**, 5894 (2014).
[12] M. J. Kim, J. C. Bird, A. J. Van Parys, K. S. Breuer, and T. R. Powers, P. Natl. Acad. Sci. USA **100**, 15481

(2003).
[13] M. J. Kim, M. J. Kim, J. C. Bird, J. Park, T. R. Powers, and K. S. Breuer, Exp. Fluids **37**, 782 (2004).
[14] H. Flores, E. Lobaton, S. Mendez-Diez, S. Tlupova, and R. Cortez, B. Math. Biol. **67**, 137 (2005).
[15] S. Y. Reigh, R. G. Winkler, and G. Gompper, Soft Matter **8**, 4363 (2012).
[16] S. Y. Reigh, R. G. Winkler, and G. Gompper, PLoS One **8** (2013), 10.1371/journal.pone.0070868.
[17] M. J. Kim and T. R. Powers, Phys. Rev. E **69** (2004), 10.1103/PhysRevE.69.061910.
[18] M. Reichert and H. Stark, Eur. Phys. J. E **17**, 493 (2005).
[19] S. H. Strogatz, Physica D **143**, 1 (2000).
[20] J. A. Acebron, L. L. Bonilla, C. J. P. Vicente, F. Ritort, and R. Spigler, Rev. Mod. Phys. **77**, 137 (2005).
[21] F. Dörfler and F. Bullo, in *Proceedings of the 51st IEEE Conference on Decision and Control* (Maui, Hawaii, USA, 2012).
[22] P. Lenz and A. Ryskin, Phys. Biol. **3**, 285 (2006).
[23] A. Vilfan and F. Julicher, Phys. Rev. Lett. **96** (2006), 10.1103/PhysRevLett.96.058102.
[24] B. Guirao and J.-F. Joanny, Biophys. J. **92**, 1900 (2007).

[25] E. M. Purcell, Am. J. Phys. **45**, 3 (1977).

[26] G. K. Batchelor, *An Introduction to Fluid Mechanics* (Cambridge University Press, Cambridge, UK, 1967).

[27] C. Pozrikidis, *Boundary Integral and Singularity Methods for Linearized Viscous Flow* (Cambridge University Press, Cambridge, UK, 1992).

[28] C. Pozrikidis, *Introduction to Theoretical and Computational Fluid Dynamics* (Oxford University Press, Oxford, UK, 1997).

[29] R. Cortez, SIAM J. Sci. Comput. **23**, 1204 (2001).

[30] R. Cortez, L. Fauci, and A. Medovikov, Phys. Fluids **17** (2005), 10.1063/1.1830486.

[31] N. C. Darnton, L. Turner, S. Rojevsky, and H. C. Berg, J. Bacteriol. **189**, 1756 (2007).

[32] B. Rodenborn, C.-H. Chen, H. L. Swinney, B. Liu, and H. P. Zhang, P. Natl. Acad. Sci. USA **110**, E338 (2013).

[33] E. L. Bouzarth and M. L. Minion, J. Comput. Phys. **230**, 3929 (2011).

[34] H. C. Berg and L. Turner, Biophys. J. **65**, 2201 (1993).

[35] X. B. Chen and H. C. Berg, Biophys. J. **78**, 1036 (2000).

[36] E. Lauga, Soft Matter **7**, 3060 (2011).